

## WAKE STRUCTURES OF UNSTEADY TWO-DIMENSIONAL FLOWS PAST CYLINDERS WITH TRIANGULAR CROSS-SECTIONS

Zhi Y. NG\*, Wisam K. HUSSAM, and Gregory J. SHEARD

The Sheard Lab, Department of Mechanical Engineering, Monash University, Victoria 3800, AUSTRALIA

\*Corresponding author, E-mail address: Zhi.Ng@monash.edu

### ABSTRACT

The effects on the wakes of unsteady flows past a cylinder with sharp separation edges are investigated. Time evolution of the incompressible Navier–Stokes equations is achieved by means of a high-order spectral-element method in conjunction with a third-order-accurate time integration scheme. For this study, the Reynolds number was varied up to  $Re_h = 200$ , where  $h$  is the projected frontal height of the cylinder having an equilateral triangular cross-section. The critical Reynolds numbers for vortex shedding for the cylinder at various inclinations are determined using the Stuart–Landau equation, and its dependence on the cylinder inclination described. As the Reynolds number is increased, the Kármán vortex street is observed to first develop spatially into a bi-layered wake profile, which then, depending on the cylinder inclination, observes a transition to either a secondary meandering profile or wakes reminiscent of the 2P and P+S modes found for oscillating circular cylinders. The flow-induced forces relating to the different wake regimes are also reported.

### NOMENCLATURE

$C_D$	Drag force coefficient
$C_L$	Lift force coefficient
$D$	Cylinder side length
$h$	Projected frontal height of cylinder
$p$	Pressure
$Re$	Reynolds number scaled by $h$
$St$	Strouhal number
$\mathbf{u}$	Velocity vector $\langle u_x, u_y \rangle$
$\alpha$	Cylinder incidence angle
$\Lambda$	Signal amplitude (Stuart–Landau equation)
$\nu$	Kinematic viscosity
$\rho$	Fluid density
$\sigma$	Instability growth rate (Stuart–Landau equation)

### INTRODUCTION

Studies into the wakes of bluff-bodies continue to yield fascinating results, driving a continuing interest to uncover their physics in further detail. While early investigations on this topic focused primarily on the circular cylinder (Kármán, 1911; Taneda, 1959; Durgin and Karlsson, 1971; Mathis *et al.*, 1984; Provansal *et al.*, 1987; Cimbalá *et al.*, 1988; and many others), sufficient knowledge of the vortex dynamics of these flows have been developed to motivate the need to understand how differently these flows behave for bluff-bodies of different polygonal shapes (e.g. Sheard *et al.*, 2003; Yoon *et al.*, 2010; Thompson *et al.*, 2014).

The following describes the known wake states of flows past a stationary cylinder, mostly found for the circular cross-section. Instability leading to transition from a steady to unsteady flow has been shown to occur at a critical Reynolds number via a supercritical bifurcation. For a certain range of Reynolds numbers beyond this transition, vortex shedding is observed with the pattern of alternating two-dimensional counter-rotating vortices convecting downstream representing the Kármán vortex street (after von Kármán (1911) who studied the stability of the arrangement of the vortices in the wake). Taneda (1959) reported the shed vortices to deform as they convect downstream, causing the vortex arrangement to eventually become unstable and merge to a larger-scale vortex street – the vortex spacing playing a crucial role in the deformation mode of the vortices (Durgin and Karlsson, 1971). The formation of these large-scale vortex structures have also been reported to be strongly affected by the geometry of the cylinder, and to become more prominent with increasing Reynolds numbers (Thompson *et al.*, 2014). The importance of the Reynolds number on the resulting wake is well established.

Studies of the wake, stability, flow-induced forces and other aspects of two-dimensional flows past various other cylinder geometries demonstrate the increased interest in the fluid dynamics past non-circular cylindrical bodies (e.g. Jackson, 1987; Johnson *et al.*, 2004; Yoon *et al.*, 2010). Specifically for the stationary triangular cylinder in an unbounded flow with its apex facing upstream, Jackson (1987) and Zielinska and Wesfreid (1995) conducted stability analyses on the flow and predicted the critical Reynolds number to be 35 and 38.3 respectively, along with the corresponding critical Strouhal numbers. De and Dalal (2006) performed a similar analysis for the same triangular cylinder inclination but also included the flow-induced forces, and reported the critical Reynolds number to be 39.9. Wind-tunnel experiments by Iungo and Buresti (2009) at  $Re \approx 1.2 \times 10^5$  varied the incidence angles of triangular cylinders of finite span and reported large variations in the mean drag and lift forces for different cylinder inclinations corresponding to changes in the wake flow features, and the trends of which appear to be similar at lower Reynolds numbers of 100 and 150 for a cylinder of infinite span (Bao *et al.*, 2010). In any case, the effects of intermediate triangular cylinder inclinations on the wake stability and flow dynamics have yet to be investigated. This study addresses this question using computational fluid dynamics.

## METHODOLOGY

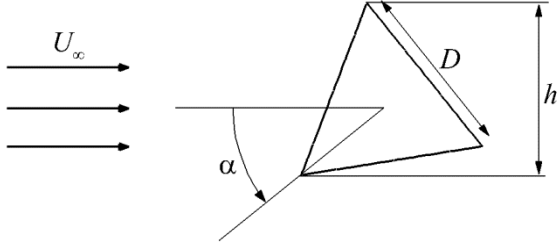


**Figure 1:** Schematic of the system under investigation.

The system under consideration (summarised in figure 1) consists of a cylinder having an equilateral triangular cross-section placed in an unbounded uniform flow. The cylinder cross-section has side length  $D$ , and is inclined at an angle  $\alpha$ , thus presenting a projected height  $h$  to the oncoming flow such that:

$$\frac{h}{D}(\alpha) = \sin(60^\circ - |\alpha - 30^\circ|) + \sin(|\alpha - 30^\circ|).$$

For this study, the velocities are scaled by the freestream velocity  $U_\infty$ , while the lengths are scaled by  $h$ , and the Reynolds number is defined as

$$Re = \frac{U_\infty h}{\nu},$$

where  $\nu$  is the kinematic viscosity.

### Numerical formulation

The relevant governing equations in this study are the Navier–Stokes equations, which for an incompressible fluid comprise mass and momentum conservation equations

$$\nabla \cdot \mathbf{u} = 0, \quad (1a)$$

$$\frac{\partial \mathbf{u}}{\partial t} + (\mathbf{u} \cdot \nabla) \mathbf{u} = -\frac{1}{\rho} \nabla p + \nu \nabla^2 \mathbf{u}, \quad (1b)$$

where  $\mathbf{u}$  is the velocity field  $\langle u_x, u_y \rangle$ ,  $p$  is the pressure, and  $\rho$  the fluid density.

The in-house solver used in this study evolves equation (1) as follows: spatial discretisation of the computational domain is achieved via a nodal spectral-element method where a Lagrangian tensor-product polynomial shape function is imposed on each macro-element and interpolated at the Gauss–Legendre–Lobatto quadrature points enabling the use of efficient quadrature methods, with the order of the polynomial shape function  $N$  being varied to control the spatial resolution (Karniadakis and Triantafyllou, 1992). The equations are then integrated in time using a third-order accurate operator splitting scheme based on backward differentiation (Karniadakis *et al.*, 1991; Blackburn and Sherwin, 2004). The advantages of the spectral-element method are its near spectral convergence properties with increasing  $N$ , and the ability to control of the mesh density over the computational domain. This code has been implemented and validated in previous studies by Sheard *et al.* (2007), Hussam *et al.* (2011), Sheard (2011), and Vo *et al.* (2014) among others.

The following boundary conditions are imposed on the computational domain, an example of which is shown in Figure 2. A uniform freestream velocity field  $(U_\infty, 0)$  is imposed on the inlet boundary (left edge), while a standard zero reference pressure outflow condition is imposed on the outlet boundary (right edge); the cylinder surface is defined with a no-slip boundary condition; and the transverse boundaries (top and bottom edges) are prescribed a stress-free impermeable condition using a zero transverse velocity component,  $u_y = 0$ , and a zero outward normal gradient of velocity,  $\partial \mathbf{u} / \partial y = 0$ . A suitable Neumann boundary

condition is enforced on the outward normal gradient of pressure on all boundaries where a Dirichlet condition is imposed on the velocity field to maintain the third-order accuracy of the time-integration scheme (Karniadakis *et al.*, 1991).

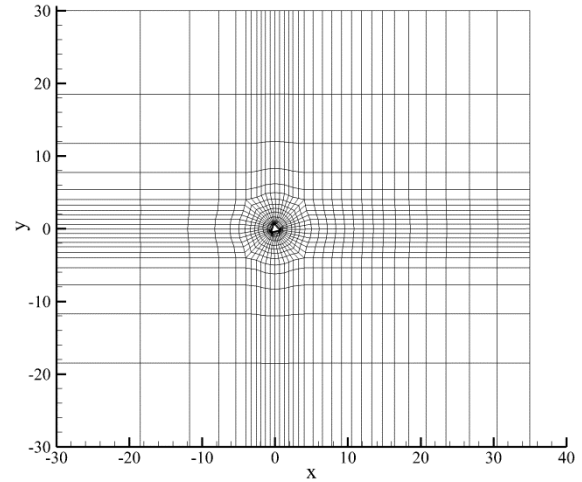


**Figure 2:** Example computational domain utilised for this study showing the macro-element distribution.

### Grid resolution study

To ensure that the meshes used in this study are sufficiently refined to capture the dynamics of the flow with sufficient accuracy, a grid refinement study is conducted by varying the polynomial order  $N$ . The mesh selected for this purpose is the cylinder inclined at  $\alpha=30^\circ$  as it possesses the largest macro-elements – the construction of the mesh defined the macro-element sizes in the vicinity of the cylinder parametrically based on the cylinder side length  $D$ , which is largest for  $\alpha=30^\circ$ . The flow for the upper bound of Reynolds numbers considered,  $Re=200$ , was then evolved to a saturated state for  $5 \leq N \leq 11$ , monitoring the Strouhal number  $St$ , time-averaged lift force coefficient  $C_L$ , time-averaged drag force coefficient  $C_D$ , and the  $L^2$ -norm of the velocity for convergence. Table 1 summarises the results for  $6 \leq N \leq 10$  with its relative errors based on the  $(N-1)^{\text{th}}$  order shown in the parentheses.

$N$	$St$	$C_D$	$C_L$	$L^2$ -norm
6	0.1692	1.9991	-1.4887	7892.0
7	0.1687 (0.296%)	1.9983 (0.040%)	-1.4861 (0.175%)	7899.7 (0.097%)
8	0.1686 (0.059%)	1.9993 (0.050%)	-1.4873 (0.081%)	7901.3 (0.021%)
9	0.1685 (0.059%)	1.9994 (0.005%)	-1.4879 (0.040%)	7902.2 (0.011%)
10	0.1685 (0.000%)	1.9994 (0.000%)	-1.4885 (0.040%)	7902.4 (0.002%)

**Table 1:** Values of  $St$ ,  $C_D$ ,  $C_L$ , and  $L^2$ -norm as  $N$  is increased. Bracketed values are the errors of each parameter relative to the lower  $N$  value.

The output parameters monitored for  $N \geq 8$  show convergence to a precision of 0.1%, indicating that the underlying flow dynamics are sufficiently resolved. Thus, all meshes used in this study are discretised using an  $N=8$  order polynomial shape function. The computational domain extends  $30h$  upstream,  $35h$  downstream, and  $30h$  transversely on either side of the cylinder centre yielding a domain blockage ratio of 1.7% ( $1/60$ ). The computational

domain is larger than most previous numerical studies referenced to minimize domain effects on the flow.

## RESULTS

### Unsteady flow past the cylinder

To map the unsteady flow regime, the critical Reynolds numbers for various cylinder inclinations is first studied. This transition being of a Hopf type is accurately modelled by the Stuart–Landau equation, which describes the non-linear growth of a perturbation in the flow field; Mathis *et al.* (1984), Provansal *et al.* (1987) and Sreenivasan *et al.* (1987) showed this transition to be supercritical for circular cylinders. Retaining only the first two terms of the real component of the Stuart–Landau equation yields

$$\frac{d(\log|\Lambda|)}{dt} = \sigma + l|\Lambda|^2, \quad (2)$$

where  $|\Lambda|$  is the magnitude of the signal amplitude, and  $\sigma$  is the growth rate of the perturbation in the flow field. The  $l$  parameter in equation 2 is necessarily negative valued for supercritical Hopf bifurcations, which are sufficiently described by equation 2.

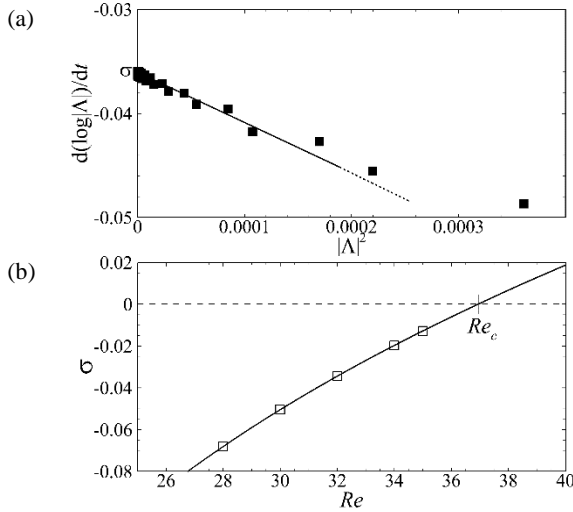


**Figure 3:** Typical plots of (a)  $d(\log|\Lambda|)/dt$  against  $|\Lambda|^2$ , and (b) the infinitesimal growth rate  $\sigma$  against the Reynolds number. The dotted line shows the zero growth rate position, while the solid line shows the fitted function extrapolated to obtain the critical Reynolds number.

The approach taken to obtain the critical Reynolds number for each flow scenario in this study was to first obtain a saturated unsteady base flow, and impose an impulsive drop in  $Re$  to allow the wake to decay to a steady state. Time histories of the transverse velocity oscillations,  $u_y$ , and the lift force coefficients,  $C_L$ , of the decay were then analysed to obtain the signal amplitude decay rate  $d(\log|\Lambda|)/dt$ , and  $|\Lambda|^2$ . Plotting these values as described in equation 2 (a typical plot of which is provided in Figure 3a) shows a nearly linear profile near the vertical axis intercept which corresponds to  $\sigma$ , and a negative gradient  $l$  indicating the transition for triangular cylinders are supercritical like the circular cylinder. A plot of the growth rate of the perturbation  $\sigma$  as a function of Reynolds number is produced, and the data trends extrapolated to a zero growth rate (marginal stability) to obtain an estimate of the critical Reynolds number,  $Re_c$ . While in some previous studies the perturbation growth rate against Reynolds number plots agreed to a linear fit (Provansal *et al.*, 1987; Sreenivasan *et al.*, 1987), the data obtained for the triangular cylinder was

evidently not linearly dependent (figure 3b). To facilitate a better prediction of the critical Reynolds numbers from the data obtained, an inverse polynomial fit was utilized for extrapolation purposes. Repeating the procedures outlined, the critical Reynolds numbers are obtained for all cylinder inclinations tested, with results shown in Figure 4.

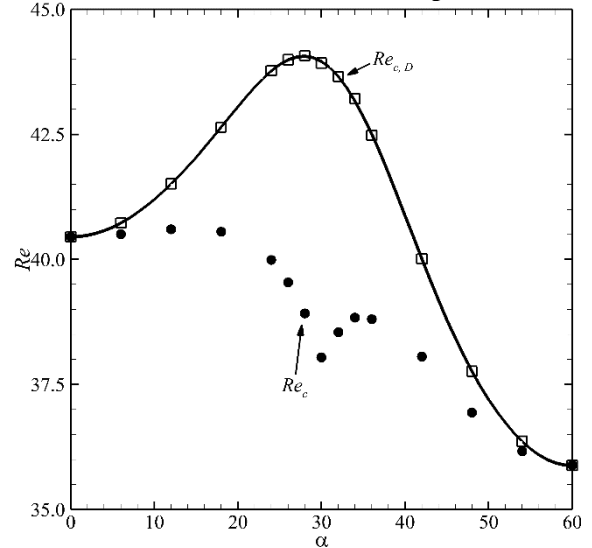


**Figure 4:** Map of the critical Reynolds number  $Re_c$  (●) and  $Re_{c,D}$  (□) as  $\alpha$  is varied. The fitted line is described by equation 3.

The critical Reynolds numbers scaled by  $D$ ,  $Re_{c,D}$  show a smooth trend, and is fitted with a Fourier function. Curve fitting for  $Re_{c,D}(\alpha)$  was performed using MATLAB®'s 'cftool' application and the resulting equation reproduced  $Re_{c,D}$  values to within 0.1% of the values obtained.

$$Re_{c,D}(\alpha) = a_0 + a_1 \cos(\omega\alpha) + b_1 \sin(\omega\alpha) + a_2 \cos(2\omega\alpha) + b_2 \sin(2\omega\alpha) + a_3 \cos(3\omega\alpha) + b_3 \sin(3\omega\alpha) + a_4 \cos(4\omega\alpha) + b_4 \sin(4\omega\alpha) \quad (3)$$

where  $a_0 = 40.067$ ,  $a_1 = 9.385 \times 10^{-1}$ ,  $a_2 = -4.588 \times 10^{-1}$ ,  $a_3 = 2.176 \times 10^{-2}$ ,  $a_4 = -1.159 \times 10^{-1}$ ,  $b_1 = 3.054$ ,  $b_2 = -1.481$ ,  $b_3 = -1.302 \times 10^{-1}$ ,  $b_4 = 8.442 \times 10^{-2}$ , and  $\omega = 3.938$ , are the coefficients of equation 3. The cylinder inclined at  $\alpha=28^\circ$  shows the highest  $Re_{c,D}$  value, and the lowest being for  $\alpha=60^\circ$ . An immediate explanation for the peak value would be to surmise that the cylinder at  $\alpha \approx 30^\circ$  possesses the smallest  $h$  relative to  $D$  of the range of inclinations making it more stable than the other inclinations, but this simple explanation does not account for the different critical Reynolds numbers for the cylinder at  $\alpha=0^\circ$  and  $\alpha=60^\circ$ , as well as the trends described by the  $Re_c$  curve. Focusing then on the  $Re_c$  curve itself, the critical Reynolds numbers for cylinder inclinations between  $0^\circ \leq \alpha \leq 18^\circ$  do not show significant differences, but produces a strong dip in the critical Reynolds numbers for  $18^\circ < \alpha \leq 30^\circ$ . We believe that this behaviour is due to the fact that at these inclination values, the cylinder presents a single side of the triangle to the downstream flow and that the recirculation region forms only over this single side causing it to remain similar for the lower range of incidence angles, and the drop in the critical Reynolds number values for the higher range of inclinations as the cylinder approaches  $\alpha=30^\circ$  to be due to a developing negative  $u_x$ -velocity bubble (localised backflow) on the steeper upstream side of the triangle. For cylinder inclinations  $30^\circ < \alpha \leq 60^\circ$ , the cylinder presents two sides of the triangle to the downstream flow, and demonstrates a

small critical Reynolds number peak to occur at  $\alpha \approx 34^\circ$ . The difference between the two sides of this peak are that the cylinder inclined at  $30^\circ < \alpha \lesssim 34^\circ$  shows the recirculation region to develop over a single side of the triangle, while the recirculation region of the cylinder at inclinations of  $34^\circ \lesssim \alpha \leq 60^\circ$  develops over the two downstream facing sides of the triangle, producing a broader wake compared to all other cylinder incidence angles (Iungo and Buresti, 2009).

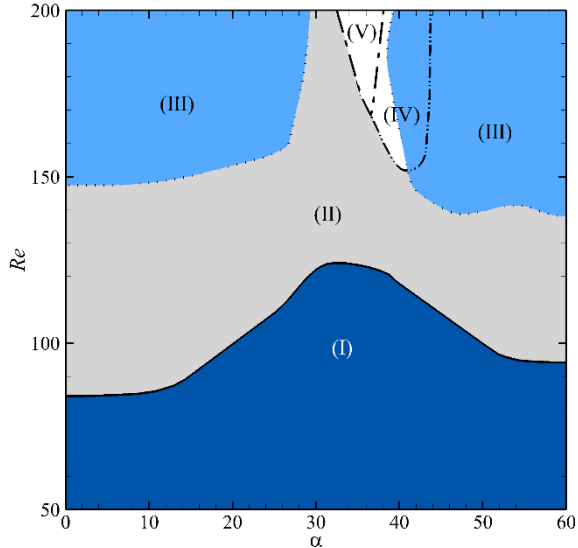


**Figure 5:** Map of the parameter space where the different vortex street shedding modes were observed. (I) is the Kármán vortex street, (II) the bi-layered vortex street, (III) the secondary vortex street, (IV) the P+S-like vortex street, and (V) the 2P-like vortex street. Note region (IV) is bounded within the  $---$ , which intersects with region (III) at higher cylinder inclinations.

At Reynolds numbers beyond  $Re_c$ , the unsteady flow develops several visually different vortex streets, the map of which is presented in figure 5 and visualisations of each vortex street encountered provided in figure 6. The initial regime encountered for increasing Reynolds numbers for all cylinder incidence angles is the classic Kármán vortex street. Increasing the Reynolds number of the flow however causes the Kármán street, at some position downstream of the cylinder, to re-align into a bi-layered wake structure due to the deformation of the vortices into an elliptical form, the major axis of each vortex aligning with other like-signed vortices (Durgin and Karlsson, 1971). For most cylinder inclinations at even higher Reynolds numbers, this bi-layered wake is further destabilised downstream and begins to distort, forming a secondary vortex street of a much larger scale than the Kármán vortex street. This is similar to the effect seen behind circular cylinders (Taneda, 1959; Durgin *et al.*, 1971; Cimbala *et al.*, 1988) and elliptical cylinders (Johnson *et al.*, 2004; Thompson *et al.*, 2014). As the frequency ratio of the near-wake to the far-wake structures shows no clear relation, the secondary vortex street does not develop by the merging of the primary vortices (Cimbala *et al.*, 1988). The development of the bi-layered vortex street and the secondary vortex street may possibly be observed at Reynolds numbers lower than those predicted in figure 5 since these structures develop at increasing distances downstream from the cylinder at progressively lower Reynolds numbers, with the current study limiting the downstream domain length to  $35h$ . These vortex streets are

formally produced by 2S modes as two counter-rotating vortices are shed per shedding cycle, with the Kármán vortex street dominating the near wake shedding for most cylinder inclinations.

For the cylinder inclination range of  $30^\circ < \alpha < 54^\circ$ , the bi-layered vortex street is shown to develop differently when the Reynolds number is further increased. The cylinder inclined at  $30^\circ < \alpha < 42^\circ$  produced a vortex street resembling that produced by the 2P shedding mode for oscillating circular cylinders, while cylinder inclinations  $42^\circ < \alpha < 54^\circ$  showed the vortex street to resemble that produced by the P+S shedding mode instead (Williamson and Roshko, 1988), with both the 2P-like and P+S-like modes differing to the actual 2P and P+S modes by the order in which the vortices are shed.

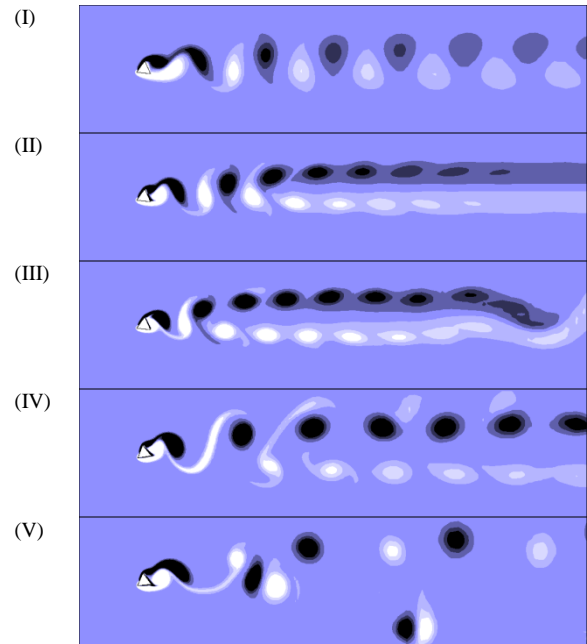


**Figure 6:** Vorticity contours of (I) the Kármán vortex street, (II) the bi-layered vortex street, (III) the secondary vortex street, (IV) the P+S-like mode, and (V) the 2P-like mode. Each image label corresponds to the same labelled regime in figure 5.

#### Forces induced on the cylinder

Analysis of the time-averaged force coefficients for the different cylinder inclinations and Reynolds numbers show trends which agree with results reported by Bao *et al.* (2010) and Iungo and Buresti (2009) despite the latter conducting experiments at much higher Reynolds numbers. The force coefficients reported in this section are thus scaled by the cylinder side length  $D$  for direct comparison with their results. For fixed Reynolds numbers and increasing the cylinder inclination from  $0^\circ$  to  $60^\circ$ , the time-averaged drag force coefficients show a minimum at an inclination of  $\alpha \approx 30^\circ$  and a maximum at  $\alpha = 60^\circ$  – the higher drag force coefficients obtained for higher incidence angles are observed to arise from the broader wakes produced at these angles (Iungo and Buresti, 2009). The time-averaged lift force coefficients instead indicate that maximum forcing occurs for the cylinder inclined at  $\alpha = 30^\circ$ , and seem negligible for cylinder inclinations  $\alpha = 0^\circ$  and  $\alpha = 60^\circ$  due to the fluctuation magnitudes being symmetric about the mean (Figure 9(bottom)).

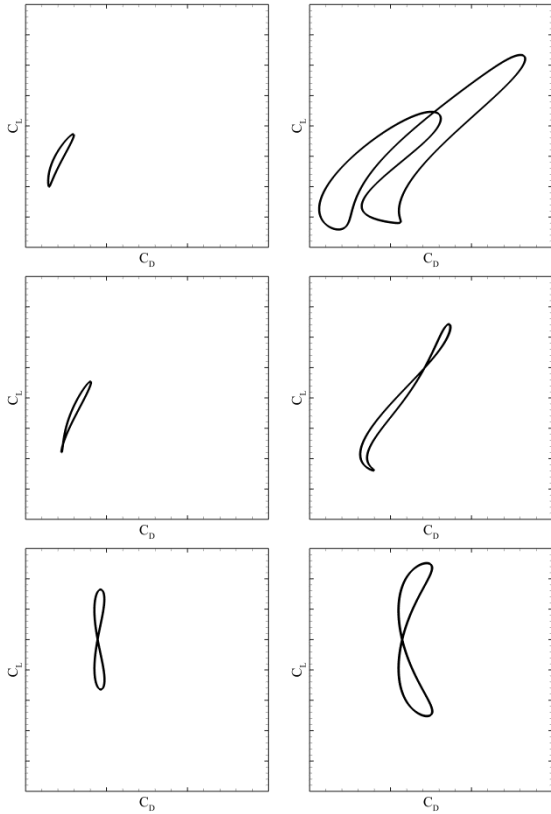


**Figure 7:** Phase of the lift forces to the drag forces for the cylinder inclined at (top)  $\alpha=36^\circ$ , (middle)  $\alpha=42^\circ$ , (bottom)  $\alpha=60^\circ$ , with the plots on the left being at  $Re=80$  (all describing the Kármán vortex street) and the plots on the right being at  $Re=200$  (describing the 2P-like mode, the P+S-like mode, and the secondary vortex street, respectively). The axis range for each plot is defined such that  $0.75 \leq C_D \leq 1.50$  and  $-1.25 \leq C_L \leq 0.75$ .

The motivation for considering the force coefficients in this study, however, was to determine if the transition to the different shedding modes incurred any changes to the force profiles. For the cylinder inclined at  $\alpha=36^\circ$  (figure 7(top)), the phase trajectory of the instantaneous force coefficients shows that the onset of the 2P-like mode alters the profile entirely. This change in the phase trajectory profile, however, was not observed for the cylinders inclined at  $\alpha=42^\circ$  (figure 7(middle)) and  $\alpha=60^\circ$  (figure 7(bottom)) – the non 2P-like shedding modes being formally 2S modes, including the P+S-like vortex street.

As observed from the phase trajectories, the asymmetric cylinder inclinations  $\alpha=36^\circ$  and  $\alpha=42^\circ$  show a biased profile compared to the cylinder inclined at  $\alpha=60^\circ$ . For  $\alpha=36^\circ$ , the fluctuations are observed to broaden upon the onset of the 2P-like mode despite having little effect on its time-averaged force coefficients (figures 8a and 9a). This broadening of the force fluctuations in the profile were not observed for cylinders at incidence angles  $\alpha=42^\circ$  and  $\alpha=60^\circ$  (figures 8b,c and 9b,c); the  $\alpha=42^\circ$  profile shows an increase in the drag force coefficients to  $Re \approx 130$  and a decreasing trend thereafter, while the lift force increases more steeply past this Reynolds number.

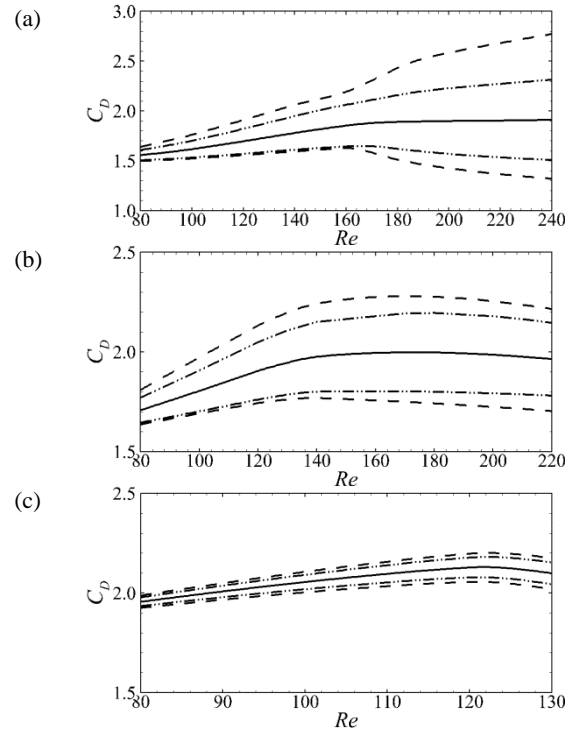


**Figure 8:** Plots of the drag force coefficients against  $Re$  for cylinder inclinations: (a)  $36^\circ$ , (b)  $42^\circ$ , and (c)  $60^\circ$ . Time-averaged force coefficients are given by the solid line, the extrema of the fluctuations by the dashed lines, and the r.m.s. of the fluctuations about the time-averaged value given by the (— · —) line.

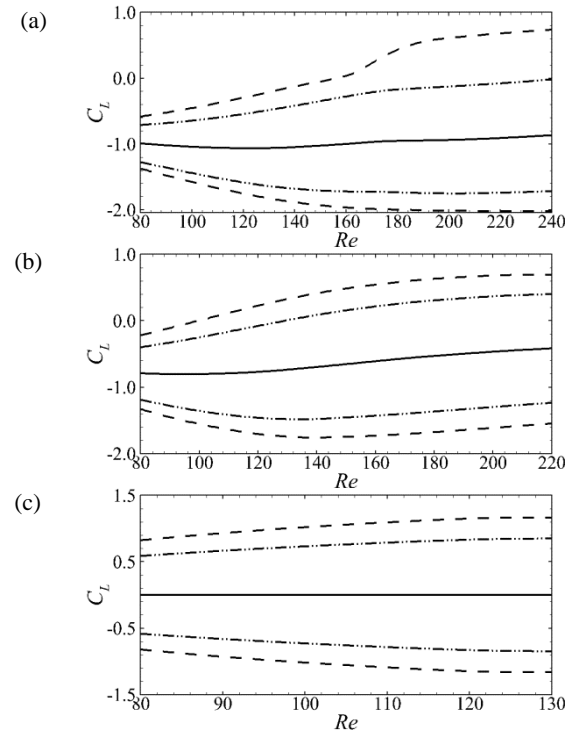


**Figure 9:** Plots of the lift force coefficients against  $Re$  for cylinder inclinations: (a)  $36^\circ$ , (b)  $42^\circ$ , and (c)  $60^\circ$ . The different lines follow the definitions in figure 8.

The Reynolds number where this drop in the drag force coefficient occurs for  $\alpha=42^\circ$  was not the Reynolds number for the transition from the Kármán vortex street to the bi-layered vortex street (the bi-layered wake was already well observed at that Reynolds number). The fluctuations of the

lift force coefficients for the cylinder inclined at  $\alpha=60^\circ$  showed very small changes for increasing Reynolds numbers indicating the lift forcing might be near a  $Re$ -independent state.

## CONCLUSION

The parameter space for the unsteady flow past a cylinder of triangular cross-section was explored for varying cylinder inclinations and Reynolds numbers up to  $Re=200$ . The critical Reynolds numbers were determined, showing the strong dependence of the instability to the cylinder inclination, with smaller  $\alpha$  generally having higher critical Reynolds numbers. The two-dimensional unsteady flows at higher Reynolds numbers are reported, with the wake structures developing from the classic Kármán vortex street to a bi-layered wake profile, and then to either of a secondary vortex street of larger-scaled structures, a 2P-like vortex street or a P+S-like vortex street depending on the incidence angle of the cylinder. The forces induced on the cylinder for the different wakes observed are described in a time-averaged sense, and the strengths of the fluctuations of the force signals are quantified. The phase-trajectory of the drag force to the lift force shows the transition from the 2S mode to the 2P-like mode to produce a strongly different profile, unlike the transitions to the other vortex streets which remain similar for increasing Reynolds numbers. The transition to the 2P-like mode (shown for  $\alpha=36^\circ$ ) also describes an abrupt change in the drag and lift force profiles as  $Re$  is increased, indicating the dominant effect of the near wake shedding mode on the forces produced.

## REFERENCES

- BAO, Y., ZHOU, D. and ZHAO, Y., (2010), "A two-step Taylor-characteristic-based Galerkin method for incompressible flows and its application to flow over triangular cylinder with different incidence angles", *Int. J. Numer. Meth. Fl.* **62**, 1181–1208.
- BLACKBURN, H. M. and SHERWIN, S. J., (2004), "Formulation of a Galerkin spectral element-Fourier method for three-dimensional incompressible flows in cylindrical geometries", *J. Comput. Phys.* **197**, 759–778.
- CIMBALA, J. M., NAGIB, H. M. and ROSHKO, A., (1988), "Large structure in the far wakes of two-dimensional bluff bodies", *J. Fluid Mech.* **190**, 265–298.
- DE, A. K. and DALAL, A., (2006), "Numerical simulation of unconfined flow past a triangular cylinder", *Int. J. Numer. Meth. Fl.* **52**, 801–821.
- DURGIN, W. W. and KARLSSON, S. K. F., (1971), "On the phenomenon of vortex street breakdown", *J. Fluid Mech.* **48**, 507–527.
- HUSSAM, W. K., THOMPSON, M. C. and SHEARD, G. J., (2011), "Dynamics and heat transfer in a quasi-two-dimensional MHD flow past a circular cylinder in a duct at high Hartmann number", *Int. J. Heat Mass Trans.* **54**, 1091–1100.
- IUNGO, G. V. and BURESTI, G., (2009), "Experimental investigation on the aerodynamic loads and wake flow features of low aspect-ratio triangular prisms at different wind directions", *J. Fluids Struct.* **25**, 1119–1135.
- JACKSON, C. P., (1987), "A finite-element study of the onset of vortex shedding in flow past variously shaped bodies", *J. Fluid Mech.* **182**, 23–45.
- JOHNSON, S. A., THOMPSON, M. C. and HOURIGAN, K., (2004), "Predicted low frequency structures in the wake of elliptical cylinders", *Eur. J. Mech. B/Fluid.* **23**, 229–239.
- VON KÁRMÁN, T., (1911), "Über den Mechanismus des Widerstandes, den ein bewegter Körper in einer Flüssigkeit erfährt", *Göttingen Nachrichten, mathematisch-physikalische Klasse*, 509–517.
- KARNIADAKIS, G. E., ISRAELI, M. and ORSZAG, S. A., (1991), "High-order splitting methods for the incompressible Navier–Stokes equations", *J. Comput. Phys.* **97**, 414–443.
- KARNIADAKIS, G. E. and TRIANTAFYLLOU, G. S., (1992), "Three-dimensional dynamics and transition to turbulence in the wake of bluff objects", *J. Fluid Mech.* **238**, 1–30.
- MATHIS, C., PROVANSAL, M. and BOYER, L., (1984), "The Bénard–von Kármán instability: an experimental study near the threshold", *J. Physique Lett.* **45**, 483–491.
- PROVANSAL, M., MATHIS, C. and BOYER, L., (1987), "Bénard–von Kármán instability: transient and forced regimes", *J. Fluid Mech.* **182**, 1–22.
- SHEARD, G. J., THOMPSON, M. C. and HOURIGAN, K., (2003), "From spheres to circular cylinders: the stability and flow structures of bluff ring wakes", *J. Fluid Mech.* **492**, 147–180.
- SHEARD, G. J., LEWEKE, T., THOMPSON, M. C. and HOURIGAN, K., (2007), "Flow around an impulsively arrested circular cylinder", *Phys. Fluids* **19**, 083601.
- SHEARD, G. J., (2011), "Wake stability features behind a square cylinder: Focus on small incidence angles", *Journal of Fluids and Structures*, **27**, 734–742.
- SREENIVASAN, K. R., STRYKOWSKI, P. J. and OLINGER, D. J., (1987), "Hopf bifurcation, Landau equation, and vortex shedding behind circular cylinders", In: *Forum on Unsteady Flow Separation*, edited by Ghia, K. N. (American Society of Mechanical Engineers), Vol. 52, pp. 1–13.
- TANEDA, S., (1959), "Downstream development of the wakes behind cylinders", *J. Phys. Soc. Jpn.* **14**, 843–848.
- THOMPSON, M. C., RADI, A., RAO, A., SHERIDAN, J. and HOURIGAN, K., (2014), "Low-Reynolds-number wakes of elliptical cylinders: from the circular cylinder to the normal flat plate", *J. Fluid Mech.* **751**, 570–600.
- VO, T., MONTABONE, L. and SHEARD, G. J., (2014), "Linear stability analysis of a shear layer induced by differential coaxial rotation within a cylindrical enclosure", *J. Fluid Mech.* **738**, 299–334.
- WILLIAMSON, C. H. K. and ROSHKO, A., (1988), "Vortex formation in the wake of an oscillating cylinder", *J. Fluids Struct.* **2**, 355–381.
- YOON, D. H., YANG, K. S. and CHOI, C. B., (2010), "Flow past a square cylinder with an angle of incidence", *Phys. Fluids* **22**, 043603.
- ZIELINSKA, B. J. A. and WESFREID, J. E., (1995), "On the spatial structure of global modes in wake flow", *Phys. Fluids* **7**, 1418–1424.